



# Photonic Crystal Ring Resonators: Characteristics and Applications\*

Zexuan Qiang<sup>1,2</sup>, Richard A. Soref<sup>3,\*</sup>, and Weidong Zhou<sup>1,\*</sup>

<sup>1</sup>Department of Electrical Engineering, NanoFAB Center, University of Texas at Arlington, Arlington, TX 76019-0072, USA

<sup>2</sup>School of Physics and Optoelectronics Technology, Fujian Normal University, Fuzhou, Fujian 350007, P. R. China

<sup>3</sup>Sensors Directorate, Air Force Research Laboratory, AFRL/RYNC, Hanscom Air Force Base, MA 01731-2909, USA

We review the characteristics and applications of photonic crystal ring resonators (PCRRs), which can potentially provide a good alternative to the traditional micro ring resonators, as one of the key contributors to the emerging low-power nanophotonic technology. Applying numerical analysis together with the theory of mode superposition, the properties of PCRRs have been comprehensively investigated. We will report PCRR key characteristics, including diameter ( $D$ )-dependent loss, quality factor ( $Q$ ), and free spectral range (FSR). No size-dependent loss was found in PCRRs, unlike the  $\sim 1/D$  dependent loss in micro-strip resonators, making PCRRs a promising candidate for ultra-compact ring resonators.

**Keywords:** Ring Resonators, Photonic Crystal, Photonic Bandgap, Mode Superposition, FDTD, Propagation Loss, Add-Drop Filter.

## CONTENTS

1. Introduction .....	1495
2. Principle and Characteristics of Compact PCRRs .....	1497
2.1. Single-Ring PCRRs .....	1498
2.2. Dual-Ring PCRRs .....	1500
2.3. Estimates of Size Dependent Insertion Loss .....	1501
3. PCRR Applications .....	1504
3.1. Nanophotonic Applications: $N \times N$ Switching .....	1504
3.2. Hybrid Silicon-Polymer Modulator .....	1505
4. Conclusions .....	1506
Acknowledgments .....	1506
References and Notes .....	1506

## 1. INTRODUCTION

Ring resonators, owing to their high spectral selectivity and large free spectral range (FSR), have been widely introduced in a wide range of device applications including linear, passive devices (such as filters,<sup>1</sup> dispersion compensators,<sup>2</sup> and sensors<sup>3</sup>) and active devices (such as modulators,<sup>4</sup> switches<sup>5</sup> and lasers,<sup>6</sup>) as well as nonlinear devices for cavity quantum electrodynamics.<sup>7</sup> To date, ring resonators have been proposed and successfully realized in a variety of materials, as summarized in Table I, including optical fibers,<sup>1,8</sup> low index contrast dielectric materials (with material index contrast  $\Delta n < 2$ ,

e.g., silica,<sup>9</sup> polymer,<sup>10</sup>  $\text{LiNbO}_3$ ,<sup>11</sup>  $\text{Si}_3\text{N}_4$ ,<sup>12</sup>  $\text{SiON}$ ,<sup>13</sup>) and high index contrast semiconductor materials ( $\Delta n \geq 2$ , e.g., SOI,<sup>14</sup>  $\text{InGaAsP}$ ,<sup>6</sup>  $\text{AlGaAs}$ ,<sup>15</sup>  $\text{GaAs}$ <sup>16</sup>). Systems based on traditional optical fiber ring technology are bulky and incompatible with photonic integration. Thanks to the advanced micro fabrication technology, planar waveguide based integrated microring resonators, also called whispering-gallery-mode (WGM) microresonators, have attracted great attention since they provide a most compact and efficient solution for the integration of these devices on a wafer scale. Among those materials mentioned above, silicon-based components are favored because they are capable of on-chip-network integration with CMOS electronics. For example, to achieve FSR larger than the optical communication window ( $\text{FSR} > 30 \text{ nm}$  for full C-band spectral coverage), a ring radius less than  $5\text{-}\mu\text{m}$  in silicon is required.<sup>17</sup> It is worth mentioning that silicon-based resonators can be tuned effectively by free-carrier plasma effect,<sup>18</sup> but they do not have truly nonlinear optical properties.<sup>11</sup> To overcome this limitation, recently, a hybrid silicon-polymer microring structure has also been proposed.<sup>19</sup> In addition, their propagation losses increase exponentially with reduction of the ring radii. This presents a problem or “roadblock” to scaling, which in practice sets a limit on the ring radius of a few micrometers (e.g.,  $3 \mu\text{m}$ ); the performance of strip-guide microring resonators is also highly sensitive to the surface roughness and the nanoscale gap between ring resonator

\*Authors to whom correspondence should be addressed.

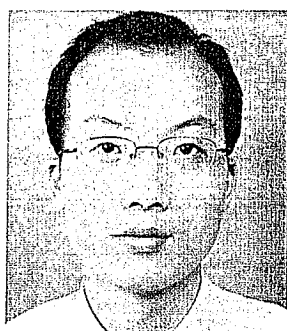
\*This is an invited review paper.

and the bus waveguide, which created another challenge in manufacturing.

On the other hand, photonic crystals (PCs) offer great promise in ultra-compact photonic components due to the unique properties associated with the PC structure, such as photonic bandgap,<sup>20</sup> guided mode resonance,<sup>21</sup> self-collimation<sup>22</sup> and superprism<sup>23</sup> etc. Within the realm of photonic crystal components, the smallest resonators reported in the literature are the point-defect resonator in a 2D crystal,<sup>24,25</sup> and the nano-scale slot within a 1D crystal.<sup>26</sup> While such devices are useful, they do

not offer the versatility of a ring-shaped PC waveguide resonator that can be coupled to bus waveguides and other rings. Recently, several types of photonic crystal ring-shaped waveguide resonator structures have been demonstrated. In the hybrid PC-waveguide structure,<sup>27</sup> the 90-degree bending section of the waveguide ring resonator is replaced with the photonic crystal reflectors, to minimize the bending loss associated with the traditional waveguides for smaller bending radius. In the PC directional coupler loop structure,<sup>28</sup> the ring miniaturization is limited by the required long coupling length, e.g.,  $80a$  as

# REVIEW



**Zexuan Qiang** received the Ph.D. degree in optical engineering from Zhejiang University in 2004. In 2004, he joined the Institute of Optical Communication of Nanjing University, Nanjing, China as an assistant professor engaged in the design and application of fiber amplifiers, fiber lasers and free space optics. In September of 2006, he joined the University of Texas at Arlington as a research assistant professor. He has also been a research faculty of Fujian Normal University, Fuzhou, China since June of 2008. His current research interests include silicon photonics for optical communications and optical sensing. He has already published more than 50 papers in the refereed national and international journals and in conference proceedings, and has three patents in China. He is also the author of a book in China (The Science Press). Dr. Qiang is a member of IEEE.



**Richard A. Soref** received the Ph.D. degree in electrical engineering from Stanford University in 1963. During 1964–65, he was a Staff Member at MIT Lincoln Laboratory and from 1965 to 1983 he was a Staff Member at the Sperry Research Center. In 1983, he joined the U. S. Air Force Research Laboratory, Hanscom AFB, where he is currently a Research Scientist in the Sensors Directorate. During his 45-year career in photonics research, he has investigated liquid-crystal devices, nonlinear optics, electro-optical switching, optical waveguide components, ferroelectric-crystal modulators, semiconductor field effects, quantum well devices, band theory and related topics. He is best known for developing and advocating the field of silicon-based photonics-and-optoelectronics. Dr. Soref holds 52 US patents, has published seven book chapters, and has authored or co-authored over 190 peer-reviewed papers. He has given numerous invited lectures and conference presentations. He has been

active in the conference committees of the Optical Society of America (OSA), Materials Research Society (MRS) and the Lasers-and-Electro-Optics Society (LEOS). In 2004, he founded the IEEE-LEOS 1st International Conference on Group IV Photonics. Richard is a Life Fellow of the IEEE and a Fellow of OSA, Air Force Research Laboratory, and the Institute of Physics UK.



**Weidong Zhou** received his B.E. and M.S. degrees from Tsinghua University, China, and Ph.D. degree from University of Michigan, Ann Arbor, all in Electrical Engineering. Currently Dr. Zhou is an Associate Professor of Electrical Engineering at University of Texas at Arlington (UTA). His current research projects include photonic crystals, infrared sensors, silicon photonics and solar cells, with funding support from US National Science Foundation, US Department of Defense Agencies (AFOSR, AFRL, ARO, DARPA) and recently a multi-million MURI center project (Multidisciplinary University Research Initiative program), etc. To date, Dr. Zhou has authored or co-authored over 120 peer reviewed journal publications, conference presentations and invited talks. He serves as various proposal and journal reviewers, and various conference committees. Dr. Zhou's major awards include prestigious *Outstanding Student of Beijing City* (Beijing, 1992), *Outstanding Graduates*

*Award* (Tsinghua Univ., Gold medal, 1993); *IEEE/LEOS Graduate Student Fellowship award* (IEEE/LEOS, 2000), *Rackham Predoctoral Fellow award* (2000–2001, Michigan), and *UTA College of Engineering Research Excellence Awards* (2007, 2008). Dr. Zhou is a senior member of IEEE, member of OSA, SPIE, MRS.

Table I. Summary of various ring resonators.

Technology	Structure/material	Characteristics		
		Ring size	Loss	Integration
Optical fiber	Fiber <sup>1,8</sup>	Large	Small	Poor
Planar waveguide	Low index contrast material ( $\Delta n < 2$ ) e.g., Silica, <sup>9</sup> polymer, <sup>10</sup> LiNbO <sub>3</sub> , <sup>11</sup> Si <sub>3</sub> N <sub>4</sub> , <sup>12</sup> SiON <sup>13</sup>	Medium	Loss increases with decrease of ring radius	Good
	High index contrast material ( $\Delta n \geq 2$ ) e.g., semiconductor material SOI, <sup>14</sup> InGaAsP, <sup>6</sup> AlGaAs, <sup>15</sup> GaAs <sup>16</sup>	Small		Good
	Hybrid e.g., polymer/Si, <sup>19</sup> Si/air slot <sup>44</sup>	Small		Good
	Hybrid PC-waveguide <sup>27</sup>	Medium	Small	Bad
Photonic crystal	PC directional coupler loop <sup>28</sup>	Medium	Small	Good
	PC self-collimation loop <sup>22</sup>	Medium	Medium	Good
	Ultra-compact PCRR <sup>30–32</sup>	Ultra-small	Small	Good

reported in Ref. [29], where  $a$  is the lattice periodicity that constrains the ring size. In the PC self-collimation loop structure<sup>22</sup> self-collimation can only exist under special propagation directions and within a certain self-collimated frequency range, e.g., the light propagates along TM direction of a square lattice structure within frequency  $[0.17a/\lambda, 0.19a/\lambda]$ .<sup>22</sup> Otherwise, it will introduce large scattering loss and thus reduce the efficiency of the device.

Recently, photonic crystal ring resonators (PCRRs)<sup>30–32</sup> have attracted great attention, for their potential in achieving ultra-compact sized ring resonators, and in flexible coupling and integration schemes. Based on photonic bandgap (PBG) confinement, ultra-compact wavelength-scale ring resonators can be fabricated in cubic, hexagonal and other complex photonic lattices.<sup>33</sup> The resonators—quasi-square, quasi rectangular, hexagonal, or circular in shape—can have a diameter as small as  $1\ \mu\text{m}$  for the operation wavelength of  $1550\ \text{nm}$ , as reported in our previous work.<sup>31,34</sup> Ultimately, the smallest PCRR can be viewed as a single point-defect PC cavity, i.e.,  $1 \times 1$  ring, which can be very low loss with extremely high quality factor ( $Q$ ), and with ultrasmall ring modal volume ( $V$ ). For various applications, the choice of PCRR ring size is determined by the desired resonant wavelength, and the tradeoffs between the quality factor  $Q$  and modal volume  $V$ .<sup>31</sup> Potentially, PCRRs present a solution to overcome the scaling obstacle of traditional WGM resonators.

In this paper, we first discuss the characteristics of the PCRRs, its principles, modal and spectral properties, followed by the demonstration of single and dual-ring resonators. The size-independent loss analysis was given with the demonstration of high performance ultra-compact add-drop filters based on single ring PCRRs. Finally, several applications based on PCRRs will be briefly described such as  $N \times N$  switching and hybrid polymer-silicon modulator.

## 2. PRINCIPLE AND CHARACTERISTICS OF COMPACT PCRRS

A traditional WGM resonator based add-drop filter (ADF) device is typically in the form of a microring closely coupled to a bus waveguide operating in single-mode, and its behavior is usually based on phase-matched coupling between orbiting waves in the ring and propagating modes in the waveguide. Similarly, an ultra-compact PCRR ADF can be formed by removing one row of PC column (W1 line defect waveguide) and a ring (or racetrack) shape of columns to perform as a bus waveguide and a compact ring resonator, respectively, as shown in Figure 1(a). In general, dielectric-rod-type PC waveguides can be easily operating in single mode while air-hole-type PC waveguides tend to be multimode without any other structure modification/optimization. Thus, for simplicity, we first consider 2D array of posts within a low-index slab, that is, dielectric-rod-type PC waveguides. Their design principles can be extended to air-hole-type ones. However, the determining principle for wavelength-size photonic crystal cavities in general can no longer be characterized as the propagating states, and the idea of phase-matching coupling may not be applicable here.<sup>24</sup> Instead, photonic-crystal resonant-cavity coupling can be analyzed based on the resonant state symmetry and degeneracy in both the real and imaginary parts of the frequency, as proposed by Fan et al.<sup>24</sup> The response of this new PCRR is numerically analyzed using a finite-difference time-domain (FDTD) approach.

Unless otherwise noted, all the discussions in this paper are based on the two-dimensional (2D) square lattice photonic-crystal structures as shown in Figure 1(a), where the refractive index of dielectric rods,  $n_h$ , is 3.48 (Silicon), surrounded by the background of air ( $n_l = 1.00$ ), the ratio of the rod radius  $r$  to the lattice period  $a$ , is 0.185. This choice is meant to simulate the behavior of a silicon-on-insulator (SOI) PC structure operating at telecomm

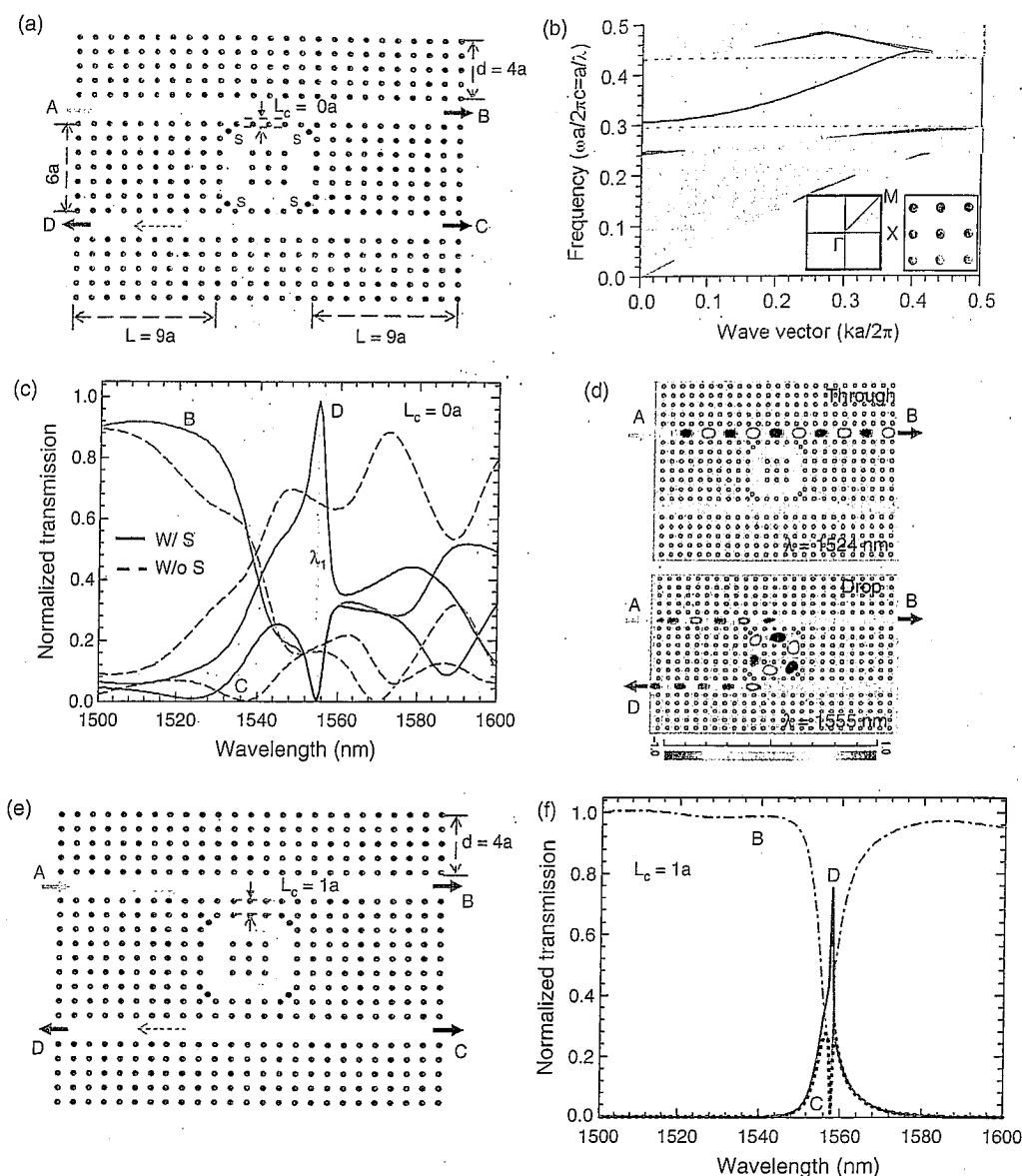


**Fig. 1.** (a) Schematic of single-ring PCRR based ADFs with coupling section  $L_c = 0a$  (one period of rods); (b) Photonic crystal dispersion plot and the corresponding defect mode (shown as a blue line) for single line defect photonic crystal waveguide (W1); (c) Normalized transmission spectra at three output ports B, C, D for PCRR ADFs with and without scatterers, 'S'; (d) The electric field patterns for the through (off-resonance:  $\lambda_0 = 1524$  nm) and drop (on-resonance:  $\lambda_1 = 1555$  nm) channels; (e) Schematic of single-ring PCRR based ADFs with increased coupling section period  $L_c = 1a$  (two periods of rods); and (f) Normalized transmission spectra with  $L_c = 1a$ .

wavelengths. Although the real SOI structure, would, in practice, require 3D numerical analysis (3D FDTD), which is typically computational time and memory consuming, our 2D approach gives a general indication of the expected 3D behavior. 2D analysis carried out here allows us to identify qualitatively many of the issues in ring cavity design (e.g., mode control and cavity  $Q$ ) and the coupling scheme design (e.g., the placement of the ring and the W1 defect waveguide, the relative coupling and symmetric impact). This can offer us the design trade-offs and guidelines for the real structure design based on a completely 3D FDTD technique.

## 2.1. Single-Ring PCRRs

A typical single-ring PCRR ADF is schematically shown in Figure 1(a). The surrounding periods of the bus waveguide (W1 Line defect waveguide, missing one row of rods along the  $\Gamma X$  direction) and ring resonator are 5 and 10, i.e.,  $d = 4a$  and  $L = 9a$ , respectively, where  $a$  is the lattice period. The coupling strength, i.e., the number of coupling periods between the bus waveguide and the PCRRs, is defined as  $L_c$ , with  $L_c = 0a$  and  $1a$  for the PCRR ADFs shown in Figures 1(a) and (e), respectively. The distance between two bus-waveguides is  $6a$ . For the PCRR ring, four extra scatterer rods, labeled as "s" in blue color, are

introduced to improve the spectral selectivity and give a near-ideal drop efficiency. Each of them is located in the center of its four nearest-neighbor rods with exactly the same diameters and refractive indices as all other dielectric rods in the PC structure. Based on the simulated photonic dispersion curve for the guided defect mode in W1 waveguide, as shown in Figure 1(b), there exists a single-mode frequency (normalized) ranging from  $0.3a/\lambda$  to  $0.428a/\lambda$ . For the 1550 nm communication window,  $a$  is set as 540 nm. Thus the W1 PC waveguide is broadband, with guided single-mode spans from 1260 to 1800 nm (between the two horizontal dash lines in Fig. 1(b)). The transmission characteristics were simulated with the two-dimensional FDTD technique using perfectly matched layers (PML) as the absorbing boundary condition. A Gaussian optical pulse, covering the whole frequency-range-of-interest, is launched at the input port A. Power monitors were placed at each of the other three ports (B, C, D) to collect the transmitted spectral power density after Fourier-transformation. All of the transmitted spectral power densities were normalized to the incident light spectral power density from input Port A.

Shown in Figure 1(c) are the normalized transmission spectra for three output ports (B, C, D) in the single-ring PCRRs. Note that, for a ring cavity *without* scatterers,

a low drop efficiency with poor spectral selectivity was obtained. By simply introducing four scatterers, significantly improved spectral selectivity with close to 100% (>99%) drop efficiency can be achieved at the resonant frequency (1555 nm in this case) as an add-drop filter (ADF). Snapshots of the electric field distribution in the ADF for through (off-resonance:  $\lambda_0 = 1524$  nm) and drop (on-resonance:  $\lambda_1 = 1555$  nm) channels are shown in Figure 1(d).

It is worth mentioning that the  $Q$  of this single-ring ADF shown in Figure 1(c) is only  $\sim 130$  ( $Q = \lambda/\delta\lambda$ ), where  $\lambda$  and  $\delta\lambda$  are the center wavelength and the linewidth (FWHM) of the drop channel, respectively. For optical communication applications, it is desirable to have a much higher  $Q$ , on the order of 1500 or higher, to achieve a linewidth of 1 nm or less. Theoretically the  $Q$  value for the ideal single-ring ( $3 \times 3$ ) PCRR can be greater than  $(10^5)^{31}$ .  $Q$  values greater than 2,000 were obtained experimentally in an air-hole-based hexagonal ring cavity laser.<sup>30</sup> The discrepancy between the ideal PCRR  $Q$  and the ADF  $Q$  is mainly caused by the coupling strength  $L_c$  in the coupling sections between the W1 waveguide and PCRR ring. As shown in Figure 1(e), higher spectral selectivity can be achieved with  $Q$  greater than 1,000 in single-ring PCRR-based ADF by simply increasing the  $L_c$  (from  $L_c = 0a$  in

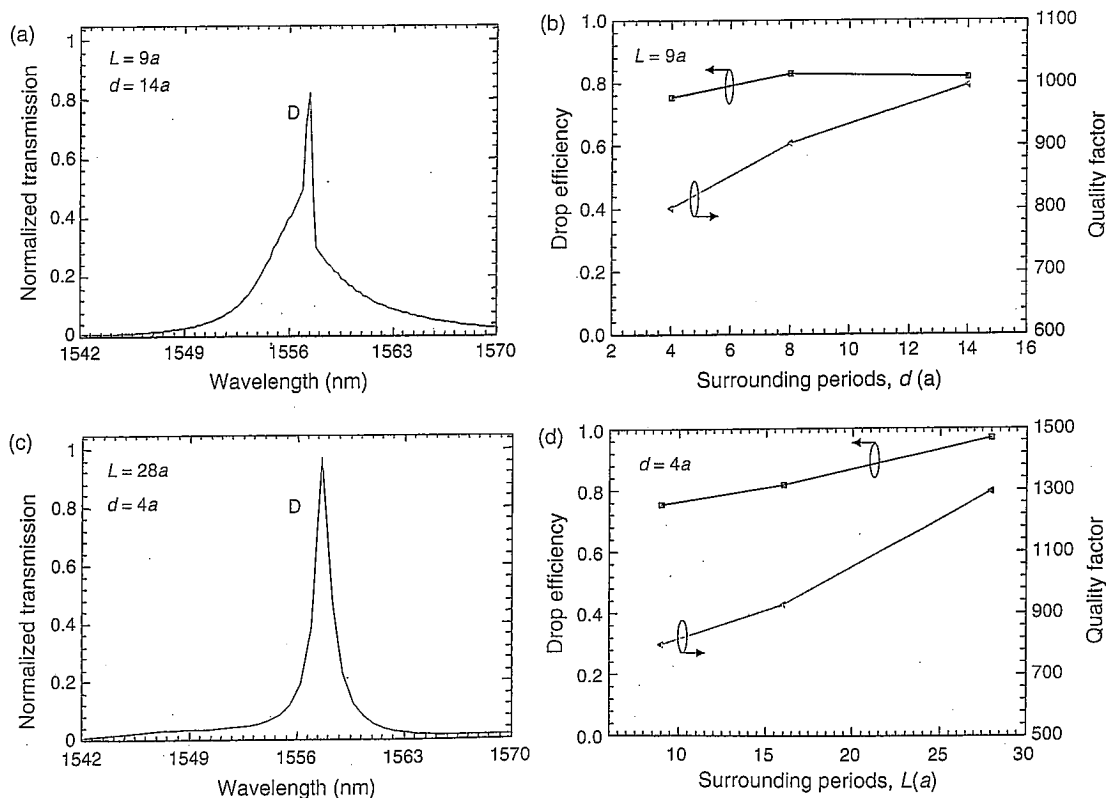


Fig. 2. The effect of surrounding periods  $d$  and  $L$  on the drop efficiency and spectral-selectivity (quality factor  $Q$ ): (a) Normalized transmission on drop channel D for  $L = 9a$  and  $d = 14a$ ; (b) Drop efficiency and spectral quality factor on drop channel D when  $d$  changes with fixed  $L = 9a$ ; (c) Normalized transmission on drop channel D for  $L = 28a$  and  $d = 4a$ ; and (d) Drop efficiency and spectral quality factor on drop channel D when  $L$  changes with fixed  $d = 4a$ .

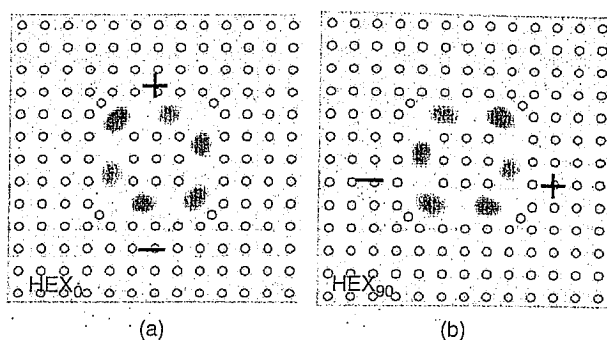


Fig. 3. The electric field patterns of PCRR cavity degenerate hexapole modes at  $\lambda = 1557.6$  nm: (a)  $\text{HEX}_0$ , and (b)  $\text{HEX}_{90}$ .

Fig. 1(c) to  $L_c = 1a$  in Fig. 1(e)). However, the dropping efficiency decreased at the same time, from 100% to 80%.

To achieve both high drop efficiency (>98%) and high spectral-selectivity, further optimization process can be considered, such as the coupling section engineering (e.g., the size of coupling rods and scatterers and location adjustment), the surrounding periods  $d$  and  $L$ , as defined in Figures 1(a, e). For example, the impacts of the surrounding periods  $d$  and  $L$  on the drop efficiency and spectral-linewidth (quality factor  $Q$ ) are investigated with the results shown in Figures 2(a, b) and (c, d), respectively. Examples of normal transmission on channel D (drop channel) is shown in Figures 2(a and c), with the drop efficiency and quality factor plots shown in Figures 2(b and d). While the impact of the surrounding period  $d$  on the drop efficiency is negligible for  $d$  greater than  $4a$  (Fig. 2(b)), spectral selectivity does increase with the increase of  $d$ , due to the improved confinement. On the other hand, both the dropping efficiency and quality factor  $Q$  increases significantly with the increase of the surrounding period  $L$  (Fig. 2(d)).

The principle of the add/drop properties in PCRRs can be explained with the mode superposition principles.<sup>24</sup> As we know, when a cavity supports degenerate modes and possesses a mirror symmetry with respect to the plane perpendicular or parallel to the waveguides, it is feasible to obtain an add-drop filter.<sup>24,33</sup> This  $3 \times 3$  PCRR supports two degenerate hexapole modes namely  $\text{HEX}_0$  and  $\text{HEX}_{90}$ , with 90-degree phase difference as illustrated in Figure 3, where  $\text{HEX}_0$  mode is even with respect to the perpendicular plane and odd with respect to the parallel plane of waveguide, while  $\text{HEX}_{90}$  mode is odd with respect to the perpendicular plane and even with respect to the parallel plane. At resonance, the resonant field couples to the drop and the input channel guides. The ring cavity power that couples back into the input guide does so in antiphase with respect to the input signal, resulting in cancellation at the throughput port and making complete power transfer from the input to the drop port possible. Based on this mode superposition principle, we can achieve even smaller ring with the same silicon rod, e.g.,  $2 \times 2$  PCRR and  $2 \times 3$  racetrack PCRR, as shown in Figure 4, where the  $L/d$  values are  $4a/9a$  and  $15a/28a$ , respectively. For easy comparison, we only discuss the performance of the  $3 \times 3$  PCRR (Fig. 1(a)) in the following sections.

## 2.2. Dual-Ring PCRRs

By cascading and coupling multiple resonators, the ADF transfer characteristics can be flexibly engineered. Forward dropping can be achieved in dual ring configurations, similar to the demonstrated schemes in the micro-ring based optical add-drop multiplexers (OADMs). Here, based on the basic building blocks of single-ring PCRRs, dual-ring PCRR-based OADMs were analyzed for both forward dropping, as well as backward dropping, with the control of mode symmetry and ring coupling.

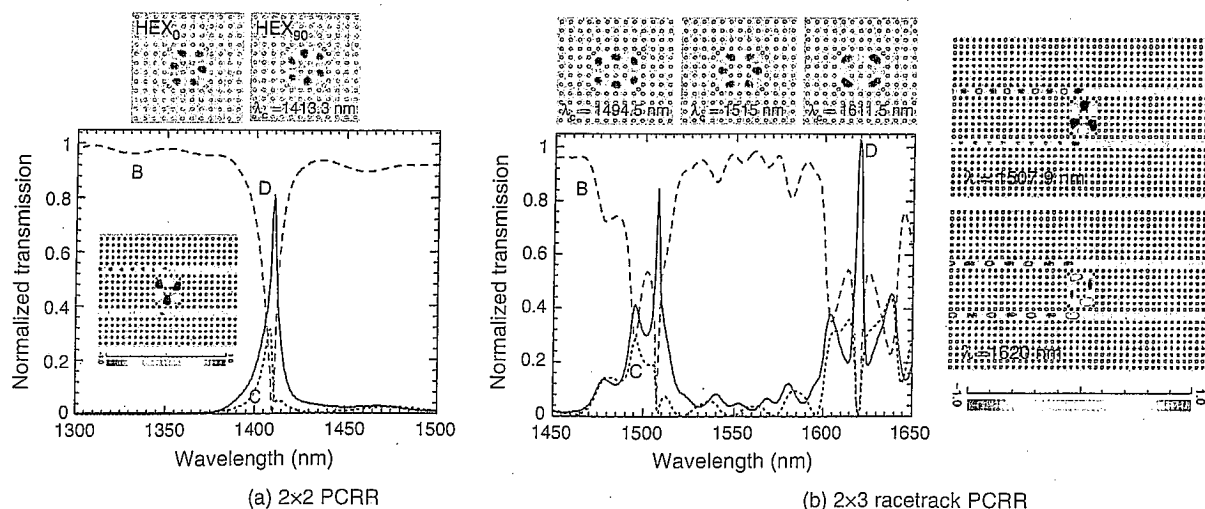


Fig. 4. Normalized transmission spectra of (a)  $2 \times 2$  PCRR; (b)  $2 \times 3$  racetrack PCRR where the top panels correspond to their intrinsic cavity resonant wavelengths.

For the weakly coupled dual ring PCRRs, as shown in Figure 5, where the total length of bus waveguide ( $L_T$ ), surrounding periods between ring resonator and bus waveguide ( $d$ ), coupling strength ( $L_c$ ) and coupling periods (defined as the number of the shared dielectric rods), were  $28a$ ,  $4a$ ,  $0a$  and  $2a$ , respectively, backward-dropping was achieved. Comparing the backward dropping characteristics shown in Figure 5(b), with the characteristics obtained from single-ring PCRRs shown in Figure 1(c), we found higher spectral selectivity was obtained with higher  $Q$  value (approaching 260) for the dropping channel in dual-ring ADFs. On the other hand, for the strong coupling case, as shown in Figure 6, where the coupling period increased to  $4a$ , forward dropping was obtained. Here the dropping channels switched to the other two resonant-cavity modes with different symmetry properties (at 1545 nm and 1561 nm). Note that this flexible design of backward and forward dropping is one of the advances in PCRRs.

Based on aforementioned mode superposition, the PCRR resonant coupling occurs due to the frequency and phase matching between the propagating waveguide mode and the PCRR resonant cavity mode. The coupling direction is mainly determined by the modal symmetry and the relative modal coupling between the PCRRs. The direction is the same for the propagating wave in the waveguide and the coupled wave inside PCRR. However, the direction may be the same or reverse for the coupling between PCRRs, depending upon the coupling strength and the modal symmetry.<sup>35</sup> Both forward dropping and backward dropping can be obtained depending upon the mode-symmetry properties with respect to the coupling configurations.

We attempted to understand this with the mode propagation animation shown in Figure 7, which shows the propagation directions for three different modes in dual-ring PCRR ADFs. In Figure 7(a), the maximum coupling

efficiency occurs at  $\lambda_1 = 1555$  nm, along  $\Gamma M$  direction, with the field minimum “-” and field maximum “+” alternatively coupled. Modes propagate clockwise in both PCRR rings, which results in backward-dropping. On the other hand, a pair of doubly degenerate modes at  $\lambda_2 = 1545$  nm and  $\lambda_3 = 1561$  nm appeared to have maximum coupling efficiency in the strongly coupled dual-ring cavities, along  $\Gamma X$  direction, where both “even-mode-like” (“+” to “+” in Fig. 7(b)) and “odd-mode-like” (“+” to “-” in Fig. 7(c)). The coupled mode in the second PCRR ring cavity propagates counter-clockwise, which leads to the forward-dropping. This opens up additional design flexibility with the desired or optimal coupling attained simply by engineering the coupling strength and modal engineering in the multi-PCRR based ADFs.

### 2.3. Estimates of Size Dependent Insertion Loss

In this section, the PCRR size-dependent loss characteristics will be discussed. For traditional micro-strip ring resonators the relationship between  $FSR$  and  $R$  is:<sup>36</sup>

$$FSR(\Delta\lambda) = \frac{\lambda^2}{(n_{\text{eff}} - \lambda \frac{\partial n_{\text{eff}}}{\partial \lambda}) \cdot 2\pi R} = \frac{\lambda^2}{n_g \cdot 2\pi R} \quad (1)$$

where  $\lambda$  is the resonant wavelength, while  $n_{\text{eff}}$  and  $n_g$  are the effective index and the group index of the ring, respectively. The group velocity can be further derived from

$$n_g = \frac{c}{v_g} = \frac{c}{d\omega/dk} \quad (2)$$

where  $c$  is the speed of light in vacuum,  $v_g$  is the group velocity, equal to  $d\omega/dk$ . We here attempted to use the same Eq. (1) to analyze the spectral characteristics of PCRR structures. The group velocity  $v_g$  can be obtained from the dispersion curve for the confined defect mode in the single-line-defect bus waveguide<sup>29</sup> after which the group index  $n_g$  is found. We first introduce an

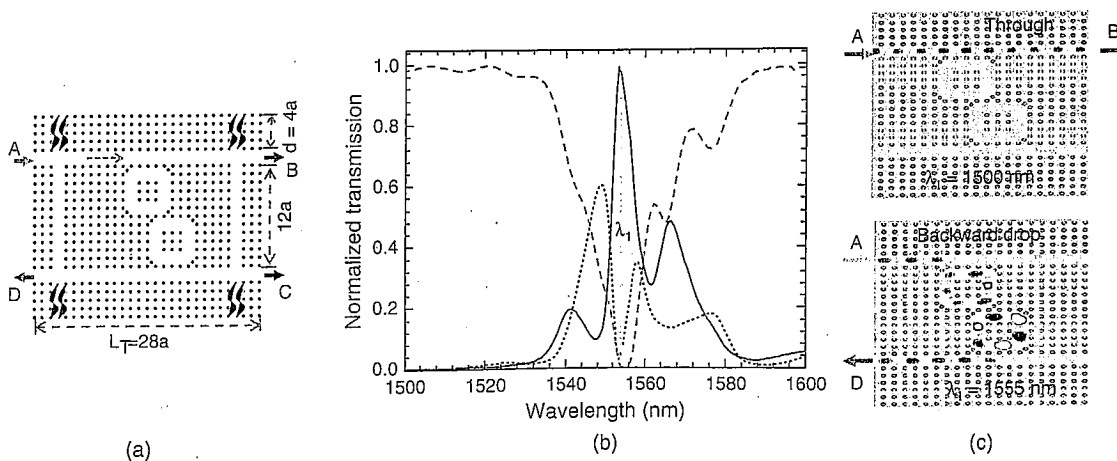


Fig. 5. Dual-ring PCRR ADFs for backward dropping (a) Schematic showing the weakly-coupled dual PCRR rings with coupling period of  $2a$ ; (b) Normalized transmission spectra; (c) The field patterns of the electric field distribution for “through” (off-resonance:  $\lambda_0 = 1500$  nm) and “backward drop” (on-resonance:  $\lambda_1 = 1555$  nm) channels. Modified with permission from [31]. Z. Qiang et al., *Opt. Express* 15, 1823 (2007). © 2007, Optical Society of America.

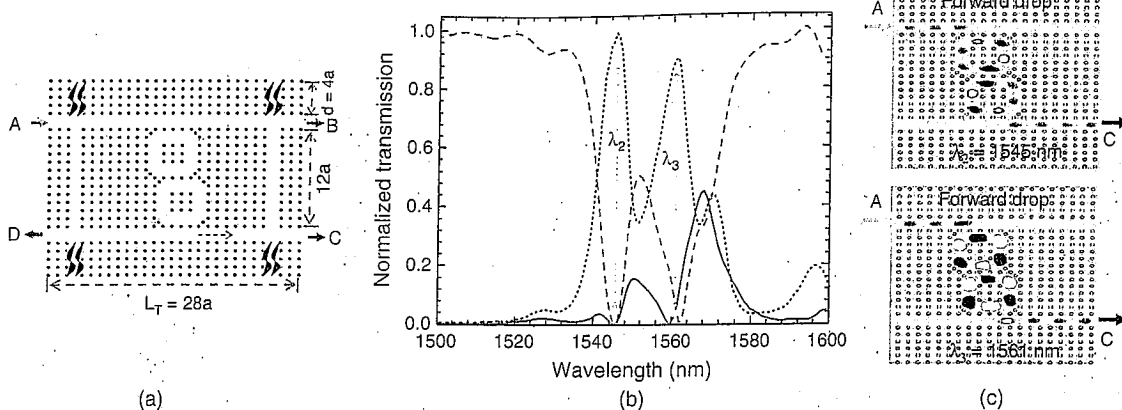


Fig. 6. Dual-ring PCRR ADFs for forward dropping (a) Schematic showing the strongly coupled dual PCRR rings with coupling period of  $4a$ ; (b) Normalized transmission spectra; (c) The field patterns of the electric field distribution for two “forward drop” channels (on-resonance:  $\lambda_2 = 1545$  nm,  $\lambda_3 = 1561$  nm). Modified with permission from [31], Z. Qiang et al., *Opt. Express* 15, 1823 (2007). © 2007, Optical Society of America.

effective radius concept for the PCRR structure based upon the equivalent area concept, as shown in Figure 9(a) (right), with

$$R_{\text{eff}} = (m + 1)a/\sqrt{\pi} \quad (3)$$

where  $m$  is the number of dielectric rods or air holes enclosed in the PCRR resonator ( $m = 3$  for the structure shown). By changing the  $m$  values, the effective radius changes accordingly. Finally, we can get the free spectral relationship of PCRRs by using the defined effective radius and the derived group index in Eq. (1).

The PCRR structure parameters of Figure 8(a) are the same as previously discussed, that is, square-lattice silicon rod surrounded by air background with  $r/a = 0.185$ . For comparison, a two-dimensional single-ring silicon micro-strip (“nano wires”) having similar configuration

parameters are used to simulate the transmission and loss properties, as shown in Figure 8(b), where the effective index and group index are both equal to 2.44, with the strip width and gap size of  $W = 500$  nm and  $t = 100$  nm, respectively. The lengths of the waveguide buses are kept the same for all cases in these two structures, which is  $L_T = 33.5$   $\mu\text{m}$  (or  $62a$  for PCRR). In the size dependent loss analysis, PCRR ADFs with different ring radius  $R$  were investigated. Based on the discussions in Section 2.1, to maintain high drop efficiency and spectral selectivity, the coupling strength,  $L_c$ , was adjusted accordingly from  $1a$  for small ring sizes (e.g., the one shown in Fig. 8(a)), to  $2a$  when the  $R_{\text{eff}}$  of PCRR increased to  $2.44$   $\mu\text{m}$  and greater ( $m > 7$ ).

Numerical simulations were carried out for PCRR and micro-strip-ring-resonator. Shown in Figure 9(a) are the

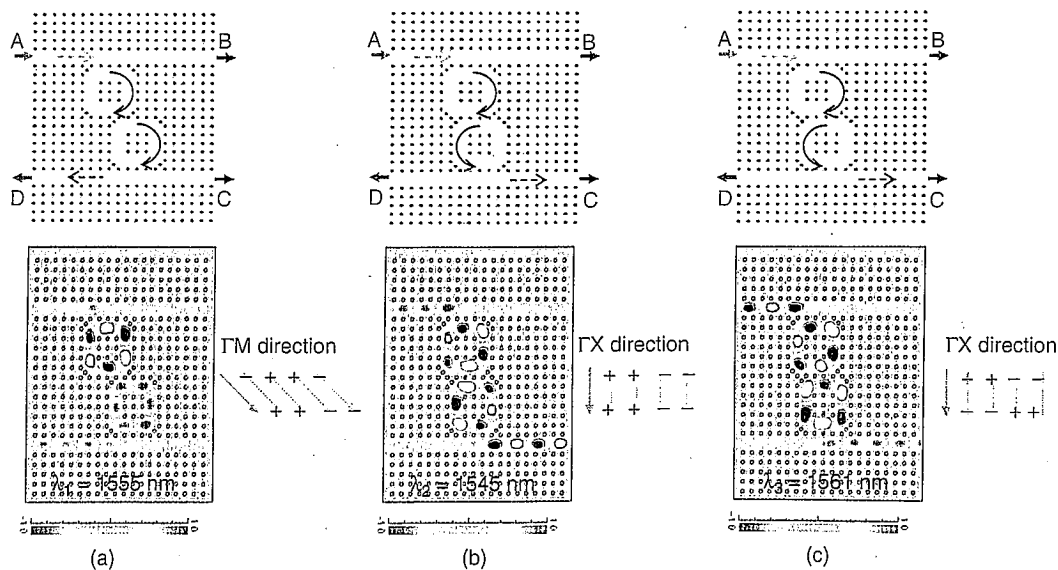


Fig. 7. Comparison of backward- and forward-dropping with the animation movies shown the different modal propagation directions due to the coupling difference and the modal symmetry. The coupling field relations are labeled with “+” and “−” signs for either even or odd modal coupling. Modified with permission from [31], Z. Qiang et al., *Opt. Express* 15, 1823 (2007). © 2007, Optical Society of America.



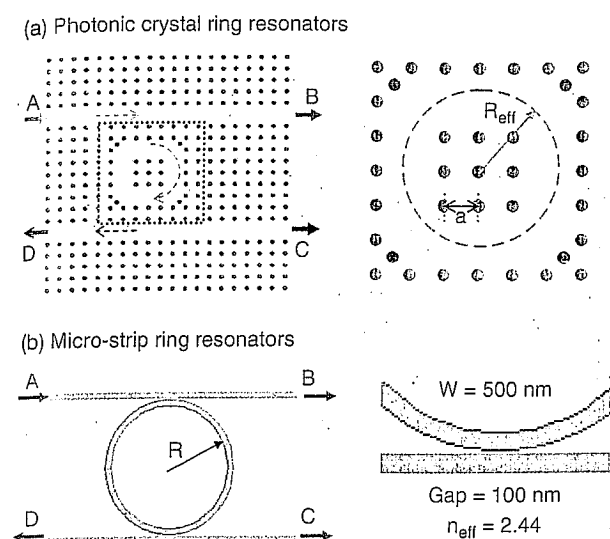


Fig. 8. (a) Schematic of photonic crystal ring resonators with effective radius  $R_{\text{eff}}$  defined as shown in the right plot; (b) Micro-strip ring resonators and the associated radius  $R$ . Reprinted with permission from [34], Z. Qiang et al., *J. Nanophotonics* 2, 023507 (2008). © (2008), SPIE.

normalized transmission spectra for three output ports (B, C, D) in the single-ring PCRR. Close to 100% drop efficiency at the drop channel of 1557.5 nm was obtained with a high spectral selectivity of  $Q$  greater than 1319 in the single ring PCRR based ADFs with 1.2- $\mu\text{m}$

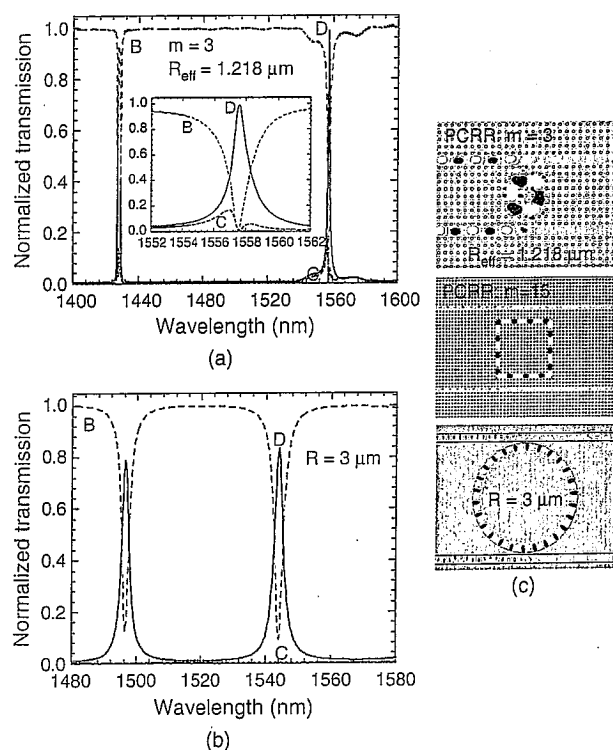


Fig. 9. Spectral response of single ring add-drop filters based on (a) PCRRs; (b) Micro-strip ring resonators; (c) The field patterns for the corresponding drop channels with different ring sizes for PCRRs and micro-strip ring resonators. Reprinted with permission from [34], Z. Qiang et al., *J. Nanophotonics* 2, 023507 (2008). © (2008), SPIE.

effective radius. We determined that the spectral performance reported here is comparable to or better than that of the micro-strip ring resonators with even large ring radius ( $R = 3 \mu\text{m}$ ), as shown in Figure 9(b). The field patterns for the drop channels with different ring sizes for PCRRs and for the micro-strip ring resonators are shown in Figure 9(c). From Figure 9(c), it is very obvious that some energy will radiate out with 3- $\mu\text{m}$  micro-strip ring resonators. Therefore, the total normalized power at three output ports  $(B + C + D)/A$  is used to derive the total bending loss in the ADF devices with different ring radii, in the unit of dB. It is worth mentioning that the total loss in the ADF devices derived here includes both the bending loss associated with small ring-radius PCRRs as well as the coupling loss between the waveguide buses and the PCRRs.

The size-dependent loss for single-ring ADFs based on the PCRR and corresponding micro-strip ring resonators is shown in Figure 10. The lower portion of loss in PCRRs is shown in the inset of Figure 10 (a zoom-in view). As expected, the bending loss increases drastically for ring radii less than 5  $\mu\text{m}$  in micro-strip ring resonators. On the other hand, we did not see any size dependent bending loss in PCRRs, which is a great advantage of proposed PCRRs. We believe the different loss behavior is due mainly to the differences in the mode confinement mechanisms.

The size-dependent free-spectral range (FSR) values were investigated and compared for both PCRRs and micro-strip ring resonators as shown in Figure 11. One set of the data plotted in Figure 11(a) is derived from the FDTD simulated spectral response curves, as shown in Figure 9, for different radii. It is interesting to note that the change in FSR associated with effective radius in PCRRs follows closely the FSR change for micro-strip-based ring resonators. By using theoretical Eqs. (1) and (2), theoretical FSR values were obtained for each radius with different

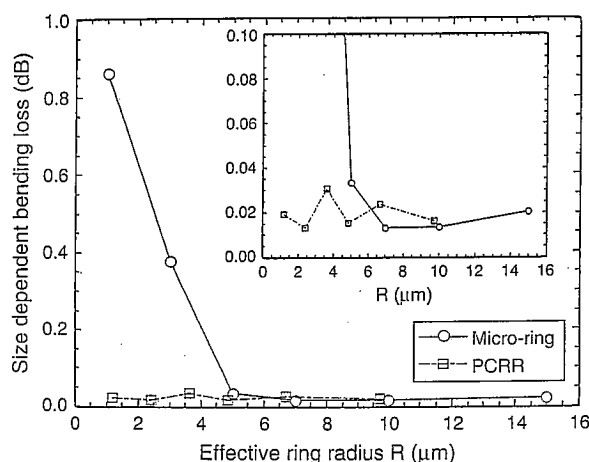


Fig. 10. Size dependent loss in PCRR and micro-strip-ring-resonator-based ADFs. The low bending loss in PCRRs is shown in the inset. Reprinted with permission from [34], Z. Qiang et al., *J. Nanophotonics* 2, 023507 (2008). © (2008), SPIE.

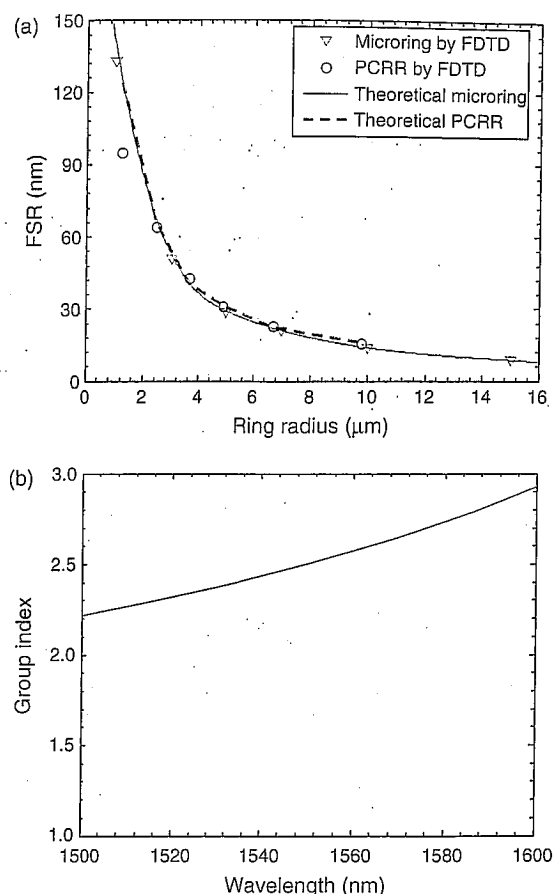


Fig. 11. (a) Size-dependent FSRs in micro-strip ring resonators and PCRRs based on FDTD simulation and theory; (b) Group index in PCRR structures based on the defect mode dispersion curve shown in Figure 1(b). Modified with permission from [34], Z. Qiang et al., *J. Nanophotonics* 2, 023507 (2008). © (2008), SPIE.

resonator wavelength and the corresponding group index shown in Figure 9(b). As shown in Figure 11(a), very good agreement was obtained between theory and FDTD simulation for both structures.

### 3. PCRR APPLICATIONS

As discussed above, PCRRs offer a potential substitute of traditional micro-ring resonators due to their advantages including flexible dropping scheme and size-independent losses for ultra-compact ring sizes. In this section, we will first conceptually provide nanophotonic applications:  $N \times N$  switching. Subsequently, we will briefly review a hybrid polymer-silicon modulator based on PCRRs.

#### 3.1. Nanophotonic Applications: $N \times N$ Switching

The small “footprint” of the PCRR allows dense integration, that is, closely packed arrays of ring devices. A prime example of such integration is the  $N \times N$  switch, which is known as a “cross connect” or  $N \times N$  “matrix switch” (see Figs. 6 and 7 of Ref. [37]) In order to illustrate the

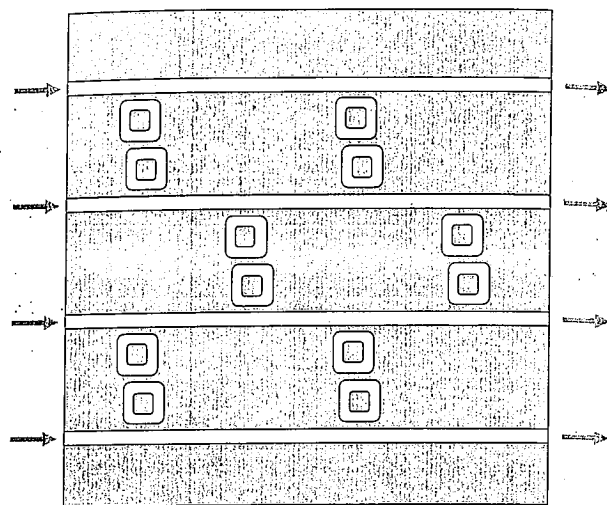


Fig. 12. A  $4 \times 4$  “permutation-matrix” switch in silicon-on-insulator based on dual ring PCRRs and line defect waveguides in a square lattice PC structure.

potential of PCRRs for dense integration, we present here the example of a  $4 \times 4$  “permutation-matrix” switch in silicon-on-insulator (a matrix discussed earlier for micro strips<sup>37</sup>). The integration approach can be monolithic or hybrid, and we shall focus here on the hybrid. The dual-ring approach is effective<sup>38</sup> and is assumed here. Starting with an SOI wafer, the first construction step would be to define lithographically a set of line-defect and ring-defect waveguides within a cubic PC lattice as shown in Figure 12. The next step would be to bond, at low temperature, an array of active III–V semiconductor dual rings, as shown in Figure 13, with these III–V waveguided PIN-diode gain media exactly aligned to the Si waveguiding regions. The cross section of one ring of a pair is shown in Figure 14, where the III–V ring guide is evanescent-wave-coupled to the Si PC guide, giving 80%

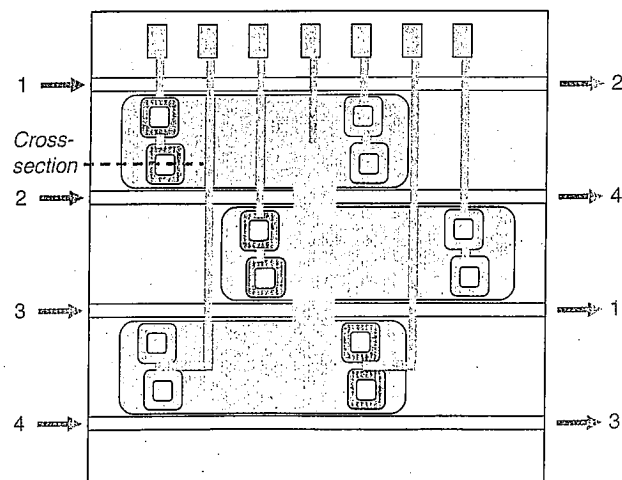


Fig. 13. An array of active III–V semiconductor dual rings is bonded to the  $4 \times 4$  “permutation-matrix” switch in silicon-on-insulator. The electrodes are shown for the switch control.

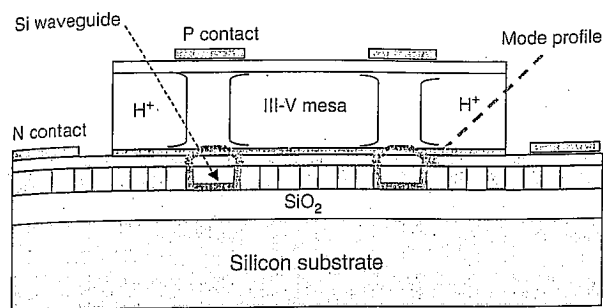


Fig. 14. The cross section of one ring of a pair is shown, where the III-V ring guide is evanescent-wave-coupled to the Si PC guide.

of the fundamental mode in Si and 20% in the III-V “active cladding.”

The Si/III-V hybrid in Figure 14 is unusual because it differs from the prior-art in which the hybrid served as a forward-biased gain medium for lasing,<sup>39</sup> or as a reverse-biased absorber for photodetection.<sup>40</sup> In the present switching case, the optical property of a ring-pair is altered—by bias switching—from a high absorption condition to a condition of optical gain. That is how the two switching states of each  $2 \times 2$  switch within the  $4 \times 4$  are attained. The III-V presents strong absorption of light at zero PIN bias. Then this cladding swings into a gain condition at forward bias. In the resonant switching art, it is known that highly

absorbing rings will produce the low-loss “bar state” of the  $2 \times 2$ , while gain within the rings provides the “cross state” also having low insertion loss.<sup>41</sup> The example of Figure 13 shows three of the six  $2 \times 2$ s forward biased, with the other three unbiased, leading to the four input-to-output pairings shown in Figure 14.

Waveguides in PCs suffer from optical scattering loss associated with wall roughness that is created during fabrication of the PC structure. This loss is “technological” rather than fundamental.<sup>42</sup> If present-day PC processing-and-smoothing techniques can be improved to the point where the waveguide losses go below 1 dB/cm, then the PCRRs described here will have performance superior to that of microstrip resonators in the small-diameter range of 4 to 10  $\lambda/n$ .

### 3.2. Hybrid Silicon-Polymer Modulator

Recently, we theoretically demonstrate a functional polymer modulator with embedded Si rods PCRR add-drop filter configuration<sup>34</sup> as shown in Figure 15, where a disruptive silicon nanomembranes (SiNM) transfer process<sup>43</sup> is used to transfer the modulator structure onto the low index ITO coated glass substrate. The vertical waveguiding structure is the polymer filled Si rods PCRR core region sandwiched in between the low index polymer cladding

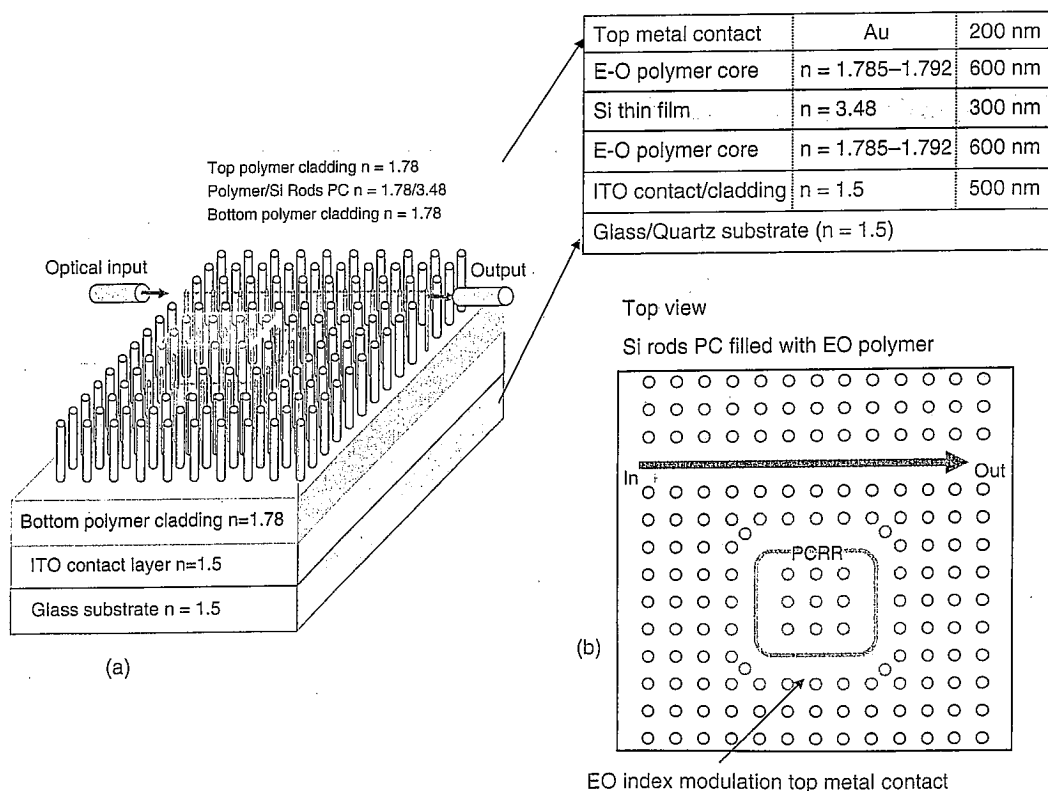


Fig. 15. Hybrid integration of functional polymers with Si PCRRs for RF photonic modulators with ultra-compact sizes: 3D, cross-sectional and top views of device structure based on Si PCRRs. Reprinted with permission from [34], Z. Qiang et al., *J. Nanophotonics* 2, 023507 (2008). © (2008), SPIE.

layers. The device design parameters used in our design is also shown in Figure 15. Electrical control is based on the bottom transparent ITO electrode and the top high speed electrode for high speed (RF frequency or greater than 100 GHz). The ON/OFF modulator is done via free carrier injection/depletion induced index change, which leads to the resonance shift.

We assume the polymer index at zero bias voltage as 1.785, based on the data for high index polymer materials from Boston Applied Technology Inc. (BATI). For an optical modulator operating at the 1.55  $\mu\text{m}$  telecommunication window, the Si rod radius  $r$  and the lattice constant  $a$  of the PC are set as 100 nm and 379 nm, respectively. Based on above Eq. (3), the effective radius of this PCRR is only 2.687  $\mu\text{m}$ , which reduces the complexity of the RF/microwave electrode design because the optical-microwave interaction region here is much less than the RF wavelength—thus affording high modulation speed. The optical channel signal propagating through W1 PC waveguide can be modulated by controlling the index of the coupled PCRR cavity region through electrical contact on top. At the ON state of the modulator, light confined by the PC structure travels along the W1 waveguide, while at the OFF state, the PCRR is tuned to resonant at the working frequency and no light passes through the W1 waveguide. By using 2D FDTD, we qualitatively identify that very high spectral selectivity can be achieved for different indices of polymers, as shown in Figure 16. For an input signal of 1565.2 nm, the modulation depth is about 25 dB with virtually 0 dB insertion loss. The corresponding propagation field patterns are shown in the inset, for ON ( $n = 1.792$ ) and OFF states. The drop channel wavelength changes from 1565.2 nm for polymer index of 1.785

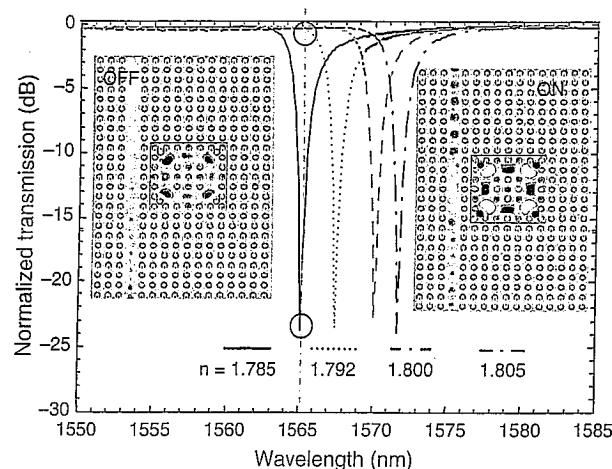


Fig. 16. Simulated spectral tuning characteristics for a single channel PC waveguide coupled with a single ring PCRRs embedded in an index tunable functional polymer material. The propagating field profiles for ON and OFF states are shown in the inset for the channel with center wavelength of 1565.2 nm at polymer indices of 1.805 and 1.785, respectively. Modified with permission from [34], Z. Qiang et al., *J. Nanophotonics* 2, 023507 (2008). © (2008), Optical Society of America.

(with zero bias voltage), to 1571.8 nm for polymer index of 1.805 (with bias voltage of a few volts).

Note that it will be very easy to create a  $2 \times 2$  EO spatial routing switch by adding simply a second ring-coupled bus waveguide on the right-hand side of the PCRR. This is an identical line-defect guide that is parallel to the bus on the left-hand side.

## 4. CONCLUSIONS

In conclusion, we have reviewed the progress of ring resonators. Emphasis has been on the principle and applications of ultra-compact photonic crystal ring resonators. We prove there is no size dependent bending losses seen in PCRR based structures. We also demonstrate that the free spectral range in PCRRs follows similar relations with effective ring radius and the dispersion related group velocity. These findings make the PCRRs an alternative to current micro-ring resonators for ultra-compact WDM components and high density photonic integration.

**Acknowledgments:** The authors acknowledge the help and support from Dr. Gernot Pomrenke. This work was supported in part by the U.S. Air Force Office of Scientific Research under Grant 07-SC-AFOSR-1004, and in part by National Science Foundation under Grant DMI-0625728.

## References and Notes

1. J. E. Bowers, S. A. Newton, W. V. Sorin, and H. J. Shaw, *Electron. Lett.* 18, 110 (1982).
2. C. K. Madsen and G. Lenz, *IEEE Photon. Technol. Lett.* 10, 994 (1998).
3. C. Y. Chao, W. Fung, and L. J. Guo, *IEEE J. Sel. Top. Quantum Electron.* 12, 134 (2006).
4. Q. Xu, S. Manipatruni, B. Schmidt, J. Shakya, and M. Lipson, *Opt. Express* 15, 430 (2007).
5. B. E. Little, H. A. Haus, J. S. Foresi, L. C. Kimerling, E. P. Ippen, and R. J. Ripin, *IEEE Photonics Technol. Lett.* 10, 816 (1998).
6. D. G. Rabus, Z. Bian, and A. Shakouri, *IEEE Photon. Technol. Lett.* 17, 1770 (1995).
7. J. Renner, L. Worschech, A. Forchel, S. Mahapatra, and K. Brunner, *Appl. Phys. Lett.* 93, 151109 (2008).
8. L. F. Stokes, M. Chodorow, and H. J. Shaw, *Opt. Lett.* 7, 288 (1982).
9. B. E. Little, S. T. Chu, P. P. Absil, J. V. Hryniewicz, F. G. Johnson, F. Seiferth, D. Gill, V. Van, O. King, and M. Trakalo, *IEEE Photon. Technol. Lett.* 16, 2263 (2004).
10. A. Leinse, M. B. J. Diemeer, A. Rousseau, and A. Driessen, *IEEE Photon. Technol. Lett.* 17, 2074 (2005).
11. A. Guarino, G. Poberaj, D. Rezzonico, R. Degl'innocenti, and P. Günter, *Nat. Photonics* 1, 407 (2007).
12. F. C. Blom, D. R. van Dijk, H. J. Hoekstra, A. Driessen, and T. J. A. Popma, *Appl. Phys. Lett.* 71, 747 (1997).
13. A. Melloni, R. Costa, P. Monguzzi, and M. Martinelli, *Opt. Lett.* 28, 1567 (2003).
14. V. R. Almeida, C. A. Barrios, R. R. Panepucci, and M. Lipson, *Nature* 431, 1081 (2004).
15. Z. Yang, P. Chak, A. D. Bristow, H. M. van Driel, R. Iyer, J. S. Aitchison, A. L. Smirl, and J. E. Sipe, *Opt. Lett.* 32, 826 (2007).
16. P. P. Absil, J. V. Hryniewicz, B. E. Little, P. S. Cho, R. A. Wilson, L. G. Joneckis, and P. Ho, *Opt. Lett.* 25, 554 (2000).

17. B. E. Little, J. Foresi, G. Steinmeyer, E. R. Thoen, S. T. Chu, H. Haus, E. Ippen, L. C. Kimberling, and W. Greene, *IEEE Photon. Technol. Lett.* 10, 549 (1998).
18. R. Soref and B. Bennett, *IEEE J. Quantum. Electron.* 23, 123 (1987).
19. K. K. McLauchlan and S. T. Dunham, *IEEE J. Sel. Top. Quantum Electron.* 12, 1455 (2006).
20. J. C. Chen, H. A. Haus, S. Fan, P. R. Villeneuve, and J. D. Joannopoulos, *IEEE J. Lightwave Technol.* 14, 2575 (1996).
21. Z. Qiang, H. Yang, L. Chen, H. Pang, Z. Ma, and W. D. Zhou, *Appl. Phys. Lett.* 93, 061106 (2008).
22. D. Zhao, C. Zhou, Q. Gong, and X. Jiang, *J. Phys. D: Appl. Phys.* 41, 115108 (2008).
23. H. Kosaka, T. Kawashima, A. Tomita, M. Notomi, T. Tamamura, T. Sato, and S. Kawakami, *Phys. Rev. B* 58, R10096 (1998).
24. S. Fan, P. R. Villeneuve, and J. D. Joannopoulos, *Opt. Express* 3, 4 (1998).
25. M. Notomi, A. Shinya, S. Mitsugi, E. Kuramochi, and H. Y. Ryu, *Opt. Express* 12, 1551 (2004).
26. J. T. Robinson, C. Manolatou, L. Chen, and M. Lipson, *Phys. Rev. Lett.* 95, 143901 (2005).
27. S. Kim, J. Cai, J. Jiang, and G. Nordin, *Opt. Express* 12, 2356 (2004).
28. V. D. Kumar, T. Srinivas, and A. Selvarajan, *Photonics and Nanostructures* 2, 199 (2004); S. H. Jeong, J. I. Sugisaka, N. Yamamoto, M. Okano, and K. Komori, *Jpn. J. Appl. Phys.* 46, L534 (2007).
29. S. H. Jeong, N. Yamamoto, J. Sugisaka, M. Okano, and K. Komori, *J. Opt. Soc. Am. B* 24, 1951 (2007).
30. S. H. Kim, H. Y. Ryu, H. G. Park, G. H. Kim, Y. S. Choi, and Y. H. Lee, *Appl. Phys. Lett.* 81, 2499 (2002).
31. Z. Qiang, W. Zhou, and R. A. Soref, *Opt. Express* 15, 1823 (2007).
32. A. R. Alija, L. J. Martinez, P. A. Postigo, C. Seassal, and P. Viktorovitch, *Appl. Phys. Lett.* 89, 101102 (2006); W. Chiu, T. Huang, Y. Wu, Y. Chan, C. Hou, H. T. Chien, and C. Chen, *Opt. Express* 15, 15500 (2007); K. Ogusu and K. Takayama, *Opt. Express* 16, 7525 (2008); M. A. Mansouri-Birjandi, M. K. Moravvej-Farshi, and A. Rostami, *Appl. Opt.* 47, 5041 (2008); P. Andalib and N. Granpayeh, *J. Opt. Soc. Am. B* 26, 10 (2009).
33. J. R. Vivas, D. Chigrin, A. Lavrinenko, and C. S. Torres, *Opt. Express* 13, 826 (2005).
34. Z. Qiang, W. D. Zhou, R. A. Soref, and Z. Ma, *J. Nanophotonics* 2, 023507 (2008).
35. K. Sakoda, *Phys. Rev. B* 52, 7982 (1995); S. H. Kim and Y. H. Lee, *IEEE J. Quantum Electron.* 39, 1081 (2003).
36. P. Rabiei, W. H. Steier, C. Zhang, and L. R. Dalton, *IEEE J. Lightwave Technol.* 20, 1968 (2002).
37. R. Soref, *IEEE J. Sel. Top. Quantum Electron.* 12, 1678 (2006).
38. S. Emelett and R. Soref, *Opt. Express* 13, 4439 (2005); S. Emelett and R. Soref, *Opt. Express* 13, 7840 (2005).
39. H. Park, A. Fang, S. Kodama, and J. Bowers, *Opt. Express* 13, 9460 (2005); J. E. Bowers, H. Park, A. W. Fang, O. Cohen, R. Jones, and M. Paniccia, *IEEE J. Sel. Top. Quantum Electron.* 12, 1657 (2006).
40. H. Park, A. W. Fang, R. Jones, O. Cohen, O. Raday, M. N. Sysak, M. J. Paniccia, and J. E. Bowers, *Opt. Express* 15, 6044 (2007).
41. R. A. Soref and B. E. Little, *IEEE Photon. Technol. Lett.* 10, 1121 (1998).
42. S. McNab, N. Moll, and Y. Vlasov, *Opt. Express* 11, 2927 (2003); Y. A. Vlasov and S. J. McNab, *Opt. Lett.* 31, 50 (2006).
43. H. C. Yuan, Z. Ma, M. M. Roberts, D. E. Savage, and M. G. Lagally, *J. Appl. Phys.* 100, 013708 (2006).
44. T. B. Jones, M. Hochberg, C. Walker, and A. Scherer, *Appl. Phys. Lett.* 86, 081101 (2005).

Received: 2 February 2009. Accepted: 31 March 2009.